PAPER

QUBIC III: Laboratory characterization

Journal of Cosmology and Astroparticle Physics
An IOP and SISSA journal

QUBIC — Q & U Bolometric Interferometer for Cosmology: instrument, current status and forecast

QUBIC III: Laboratory characterization

The QUBIC collaboration

S.A. Torchinsky,[1,2,a] J.-Ch. Hamilton,[1,a] M. Piat,[1,a] E.S. Battistelli,[3,4] P. de Bernardis,[3,4] C. Chapron,[1] G. D'Alessandro,[3,4] M. De Petris,[3,4] M.M. Gamboa Lerena,[5,33] M. González,[6] L. Grandsire,[1] S. Marnieros,[7] S. Masi,[3,4] A. Mennella,[8,9] L. Mousset,[1] J.D. Murphy,[10] C. O'Sullivan,[10] D. Prêle,[1] G. Stankowiak,[1] A. Tartari,[11] J.-P. Thermeau,[1] F. Voisin,[1] M. Zannoni,[12,13] P. Ade,[14] J.G. Alberro,[15] A. Almela,[16] G. Amico,[3] L.H. Arnaldi,[6] D. Auguste,[7] J. Aumont,[17] S. Azzoni,[18] S. Banfi,[12,13] A. Baù,[12,13] B. Bélier,[19] D. Bennett,[10] L. Bergé,[7] J.-Ph. Bernard,[17] M. Bersanelli,[8,9] M.-A. Bigot-Sazy,[1] J. Bonaparte,[20] J. Bonis,[7] E. Bunn,[21] D. Burke,[10] D. Buzi,[3] F. Cavaliere,[8,9] P. Chanial,[1] R. Charlassier,[1] A.C. Cobos Cerutti,[16] F. Columbro,[3,4] A. Coppolecchia,[3,4] G. De Gasperis,[22,23] M. De Leo,[3,24] S. Dheilly,[1] C. Duca,[16] L. Dumoulin,[7] A. Etchegoyen,[16] A. Fasciszewski,[20] L.P. Ferreyro,[16] D. Fracchia,[16] C. Franceschet,[8,9] K.M. Ganga,[1] B. García,[16] M.E. García Redondo,[16] M. Gaspard,[7] D. Gayer,[10] M. Gervasi,[12,13] M. Giard,[17] V. Gilles,[3] Y. Giraud-Heraud,[1] M. Gómez Berisso,[6] M. Gradziel,[10] M.R. Hampel,[16] D. Harari,[6] S. Henrot-Versillé,[7] F. Incardona,[8,9] E. Jules,[7] J. Kaplan,[1] C. Kristukat,[25] L. Lamagna,[3,4] S. Loucatos,[1,26] T. Louis,[7] B. Maffei,[27] W. Marty,[17] A. Mattei,[4] A. May,[28] M. McCulloch,[28] L. Mele,[3,4] D. Melo,[16] L. Montier,[17] L.M. Mundo,[15] J.A. Murphy,[10] F. Nati,[12,13] E. Olivieri,[7] C. Oriol,[7]

[a]Main author.

JCAP04(2022)036

https://doi.org/10.1088/1475-7516/2022/04/036

A. Paiella,[3,4] **F. Pajot,**[17] **A. Passerini,**[12,13] **H. Pastoriza,**[6] **A. Pelosi,**[4] **C. Perbost,**[1] **M. Perciballi,**[4] **F. Pezzotta,**[8,9] **F. Piacentini,**[3,4] **L. Piccirillo,**[28] **G. Pisano,**[14] **M. Platino,**[16] **G. Polenta,**[29] **R. Puddu,**[30] **D. Rambaud,**[17] **E. Rasztocky,**[31] **P. Ringegni,**[15] **G.E. Romero,**[31] **J.M. Salum,**[16] **A. Schillaci,**[32] **C.G. Scóccola,**[5,33] **S. Scully,**[10,34] **S. Spinelli,**[12] **M. Stolpovskiy,**[1] **A.D. Supanitsky,**[16] **P. Timbie,**[35] **M. Tomasi,**[8,9] **C. Tucker,**[14] **G. Tucker,**[36] **D. Viganò,**[8,9] **N. Vittorio,**[22] **F. Wicek,**[7] **M. Wright**[28] **and A. Zullo**[4]

[1]Astroparticule et Cosmologie, Université de Paris, CNRS,
10 Rue Alice Domon et Léonie Duquet, 75013 Paris, France

[2]Observatoire de Paris, Université Paris Science et Lettres,
61 Av. de l'Observatoire, F-75014 Paris, France

[3]Università di Roma — La Sapienza, Piazzale Aldo Moro, 5, 00185 Roma, Italy

[4]INFN sezione di Roma, Piazzale Aldo Moro, 5, 00185 Roma, Italy

[5]Facultad de Ciencias Astronómicas y Geofísicas, Universidad Nacional de La Plata,
Paseo del Bosque S/N, B1900FWA La Plata, Argentina

[6]Centro Atómico Bariloche and Instituto Balseiro (CNEA),
Av. Exequiel Bustillo 9500, San Carlos de Bariloche, Argentina

[7]Laboratoire de Physique des 2 Infinis Irène Joliot-Curie CNRS-IN2P3,
Université Paris-Saclay,
Bât. 100, 15 rue Georges Clémenceau, 91405 Orsay cedex, France

[8]Universita degli studi di Milano, Via Celoria 16, 20122 Milano, Italy

[9]INFN sezione di Milano, Via Celoria 16, 20122 Milano, Italy

[10]Department of Experimental Physics, National University of Ireland,
Maynooth, Co. Kildare, Ireland

[11]INFN — Pisa Section, Largo Bruno Pontecorvo, 3/Edificio C, 56127 Pisa, Italy

[12]Università di Milano — Bicocca, Piazza dell'Ateneo Nuovo, 1, 20126 Milano, Italy

[13]INFN Milano-Bicocca, Edificio U2, Piazza della Scienza, 3 — I-20126 Milano, Italy

[14]Cardiff University, Cardiff CF10 3AT, U.K.

[15]GEMA, Universidad Nacional de La Plata,
Calle 116 y 48, La Plata, Argentina

[16]Instituto de Tecnologías en Detección y Astropartículas (CNEA, CONICET, UNSAM),
Av. Gral Paz 1499 — San Martín, Argentina

[17]Institut de Recherche en Astrophysique et Planétologie (CNRS-INSU),
9 Av. du Colonel Roche, 31400 Toulouse, France

[18]Department of Physics, University of Oxford, Parks Rd, Oxford OX1 3PJ, U.K.

[19]Centre de Nanosciences et de Nanotechnologies,
15 Rue Georges Clémenceau, 91405 Orsay Cedex, France

[20]Centro Atómico Constituyentes (CNEA),
Av. Gral. Paz 1499, B1650 Villa Maipú, Argentina

[21]University of Richmond,
Richmond, 410 Westhampton Way, Richmond, VA 23173, U.S.A.

JCAP04(2022)036

[22]Dipartimento di fisica, Università di Roma — Tor Vergata,
Viale della Ricerca Scientifica, 1, 00133 Roma, Italy
[23]INFN sezione di Roma2, Via della Ricerca Scientifica, 1, 00133 Roma, Italy
[24]University of Surrey, Stag Hill, University Campus, Guildford GU2 7XH, U.K.
[25]Escuela de Ciencia y Tecnología (UNSAM) and Centro Atómico Constituyentes (CNEA),
Tornavías Martín de Irigoyen No.3100, B1650 Villa Lynch, Argentina
[26]IRFU, CEA, Université Paris-Saclay, Bât 141, F-91191 Gif-sur-Yvette, France
[27]Institut d'Astrophysique Spatiale, Orsay (CNRS-INSU),
Rue Jean-Dominique Cassini, 91440 Bures-sur-Yvette, France
[28]University of Manchester, Oxford Rd, Manchester M13 9PL, U.K.
[29]Italian Space Agency, Via del Politecnico snc 00133, Roma, Italy
[30]Pontificia Universidad Católica de Chile,
Av Libertador Bernardo O'Higgins 340, Santiago, Chile
[31]Instituto Argentino de Radioastronomía (CONICET, CIC),
Camino Gral. Belgrano Km 40, Berazategui, Argentina
[32]Department of Physics, California Institute of Technology, Pasadena, CA 91125, U.S.A.
[33]Consejo Nacional de Investigaciones Científicas y Técnicas (CONICET),
Godoy Cruz 2290, 1425, Ciudad Autónoma de Buenos Aires, Argentina
[34]Institute of Technology, Kilkenny Rd, Moanacurragh, Carlow, Ireland
[35]Department of Physics, University of Wisconsin Madison,
1150 University Ave, Madison WI 53703, U.S.A.
[36]Brown University, Providence, RI 02912, U.S.A.

E-mail: satorchi@apc.in2p3.fr, hamilton@apc.in2p3.fr, piat@apc.univ-paris7.fr

Received November 24, 2020
Revised February 5, 2022
Accepted March 14, 2022
Published April 21, 2022

Abstract. We report on an extensive test campaign of a prototype version of the QUBIC (Q & U Bolometric Interferometer for Cosmology) instrument, carried out at Astroparticle Physics and Cosmology (APC) in Paris. Exploiting the novel concept called bolometric interferometry, QUBIC is designed to measure the CMB polarization at 150 and 220 GHz from a high altitude site at Alto Chorillo, Argentina. The prototype model called QUBIC Technological Demonstrator (QUBIC-TD) operates in a single frequency band (150 GHz) and with a reduced number of baselines, but it contains all the elements of the QUBIC instrument in its final configuration. The test campaign included measurements of the synthesized beam and of the polarization performance, as well as a verification of the interference fringe pattern. A modulated, frequency-tunable millimetre-wave source was placed in the telescope far-field and was used to simulate a point source. The QUBIC-TD field of view was scanned across the source to produce beam maps. Our measurements confirm the frequency-dependent behaviour of the beam profile, which gives QUBIC the possibility to do spectral imaging. The measured polarization performance indicates a cross-polarization leakage less than 0.6%. We also successfully tested the polarization modulation system, which is provided by a rotating half wave plate. We demonstrate the full mapmaking pipeline using data from this measurement

JCAP04(2022)036

campaign, effectively giving an end-to-end checkout of the entire QUBIC system, including all hardware subsystems, their interfaces, and the software to operate the whole system and run the analysis. Our results confirm the viability of bolometric interferometry for measurements of the CMB polarization.

Keywords: CMBR detectors, CMBR experiments, CMBR polarisation, gravitational waves and CMBR polarization

ArXiv ePrint: 2008.10056

JCAP04(2022)036

Contents

1 Introduction

The detection of primordial B-mode polarization in the cosmic microwave background (CMB) is the subject of a worldwide effort due to its importance as a confirmation of the inflationary model of cosmology. A clear detection of polarization B-modes in the CMB at degree angular scales, distinguished from B-modes incurred by foreground effects (including lensing), is evidence of primordial gravitational waves expected during the inflationary phase in the earliest moments of the universe. For an overview see Kamionkowski & Kovetz [1].

From an observational point of view, the linear polarization of the CMB is described by the Q and U Stokes parameters than can be transformed mathematically into the scalar E and B-modes respectively corresponding to the curl and curl-free part of the polarization field on the sky. E-modes have been well measured to be of order $\sim 1\,\mu$K [2–4], as expected from the theory, while the B-mode component will be an even weaker signal, at least an order of magnitude below the E-mode [5]. As a result, the measurement of B-mode polarization is a difficult exercise of extracting a signal buried deep within other signals, be them astrophysical foregrounds or instrumental systematics mixing Q and U observables resulting into a leakage of the large E-modes into the small B-modes.

The QUBIC instrument uses a novel technology, called Bolometric Interferometry, that combines the high sensitivity offered by bolometers to the signal purity from interference fringes measurement. QUBIC has degree-scale angular resolution in order to target the primordial CMB B-mode polarization. The instrument is designed with particular attention to the limitation and control of systematic effects [6]. See also in this series of papers O'Sullivan et al. [7] for the optics design, Masi et al. [8] for the cryogenics design, and Piat et al. [9] for the detectors and readout electronics. QUBIC uses the technique of interferometry which leads to the possibility of doing "self-calibration", a procedure that

JCAP04(2022)036

ensures fine control of instrumental systematic effects [10]. Furthermore, the resulting frequency-dependent beam profile on the sky leads to the possibility of doing spectral imaging (see Mousset et al. [11] in this series of papers). Bolometric interferometry is the marriage of techniques bringing together the great sensitivity and large bandwith of bolometers and the instrumental control and high fidelity imaging of aperture synthesis. Using this innovative approach, any residual systematic effect in the data will be largely independent from those in other experiments, thus providing a unique dataset in the context of the worldwide experimental effort.

This article describes the laboratory characterization and calibration phase QUBIC has undergone. The paper is organized as follows. Section 2 gives an overview of the Q & U Bolometric Interferometer for Cosmology (QUBIC) Technological Demonstrator instrument including an introduction to the concept of bolometric interferometry. The laboratory setup is described in section 3 with particular attention given to the placement and alignment of the calibration source. This is followed by section 4 describing various measurement results and analysis. Section 4.1 presents the measured bandpass of QUBIC. Section 4.2 shows the measured response to modulated polarization using the rotating half wave plate (HWP), a critical element to assess the system polarization performance. In section 4.3 we discuss the measurement of interference fringes on the focal plane using the mechanical switches in the horn array to select baselines. In section 4.4 we show measurements of the QUBIC synthesized beam, and in section 4.5 we demonstrate the results of the QUBIC mapmaking pipeline by generating a "sky" map of the calibration source using the calibration information determined from our measurements. Finally, some concluding remarks are given in section 5.

2 The QUBIC instrument

QUBIC is an imaging interferometer which measures "visibilities" which are the complex (amplitude and phase) correlations between each antenna pair (baseline). In radio astronomy, the visibilities are recorded directly. A "correlator" digitizes the signals and multiplies pairs of signals to produce a stream of complex numbers, each of which corresponds to the cross correlation product of an antenna-pair. Channelization of the spectral bandpass permits signal processing of individual, very narrow bands, and for each channel the signal is nearly monochromatic. In radio astronomy, large bandwidths are achieved by adding more digital electronics.

2.1 Bolometric interferometry

A bolometric interferometer takes advantage of the high sensitivity and large bandwidth of bolometers while also benefiting from the calibration technique possible with an imaging interferometer. The QUBIC focal planes are populated with transition-edge sensor (TES) bolometers (see Piat et al. [9] in this special issue for more details). The spatial sampling of the sky is generated by placing a cluster of back-to-back horns that behave effectively as electromagnetic nozzles. This horn cluster creates the $u - v$ sampling of the aperture plane equivalent to what is done by a distribution of antennas in a radio array. For the bolometric interferometer, instead of sampling the signals and computing the cross correlations between antenna pairs, the interference pattern is imaged.

A single image of the interference pattern has all the information convolved together resulting in observing the sky through a synthesized beam. The shape of this synthesized beam is given by the combination of all individual baselines (all pairs of horns). The bolometric

JCAP04(2022)036

interferometer ends up being a synthesized imager observing the sky through its synthesized beam just the same way as a classical imager observes the sky through the beam formed by the telescope. For calibration and instrumental systematic effects studies it is however crucial to extract the individual visibilities. By blocking all horns except two, we would measure the interference pattern of that baseline. For technical reasons in the QUBIC Technological Demonstrator (QUBIC-TD), only two horn shutters can be shut at a time, but by making a series of measurements with different pairs of horns blocked, the result is equivalent to having all horns blocked except two [10]. The 20×20 cluster of horns in the QUBIC Full Instrument (QUBIC-FI) has 400 horns making $n(n-1)/2 = 79800$ baselines which are needed to be observed individually for self-calibration. The QUBIC-TD, whose tests are reported in this paper, has a smaller horn array with 64 horns in an 8×8 square array giving 2016 baselines.

The main parameters which determine the general performance of the bolometric interferometer are the number of baselines and the number of detectors. Performance of the bolometric interferometer improves as the number of baselines increases since this improves the application of self-calibration by increasing the number of parameters. It also leads to a more sharply defined synthesized beam. A larger cluster of horns provides more baselines, but this in turn must be sampled by a larger array of detectors in the focal plane. A larger horn cluster is also effectively a larger telescope aperture which increases the power throughput of the system. Increasing the number of detectors therefore not only improves the sampling of focal plane but also improves the sensitivity of the instrument by detecting more power. As a result, the overall performance of the bolometric interferometer is not simply a function of the number of detectors in the focal plane. It also depends on the number of baselines formed by the horn array which must be large enough to match the surface covered by detectors in the focal plane.

An additional feature of bolometric interferometry is the possibility to do spectral imaging. The synthesized beam is predicted to vary in a well-understood way with frequency. In particular, the beam secondary lobes are closer to the central lobe for higher frequency of incident radiation while the central lobe remains in the same place across the spectral band. As a result, the time ordered data (TOD) effectively samples different electromagnetic frequencies as the beam passes over the same point in the sky. An important objective of our calibration campaign was to verify this behaviour with the QUBIC-TD.

This spectral selectivity can be deconvolved in the data post processing. The spectral resolution improves with the number of baselines as the synthesized beam has finer secondary lobes with a larger cluster of horns. Spectral imaging is an innovative feature of bolometric interferometry which gives QUBIC an important advantage over other CMB imagers (see Hamilton et al. [12] and Mousset et al. [11] for details) and the expected frequency dependence of QUBIC's synthesized beam has been confirmed (see section 4.4).

2.2 Design overview

QUBIC employs an optical system consisting of back-to-back horns that select the relevant baselines and an optical combiner focusing on a bolometric focal plane. The optical combiner forms interference fringes while the bolometers average their powers over timescales much larger than the period of the light waves. This is therefore the optical equivalent of a wide-band correlator in classical interferometry. The instrument operates at cryogenic temperatures thanks to a large cryostat described in Masi et al. [8].

A schematic of the design of the QUBIC-FI is shown in figure 1 and the main instrument parameters are listed in table 1. The QUBIC-TD has the same optical layout and differs

JCAP04(2022)036

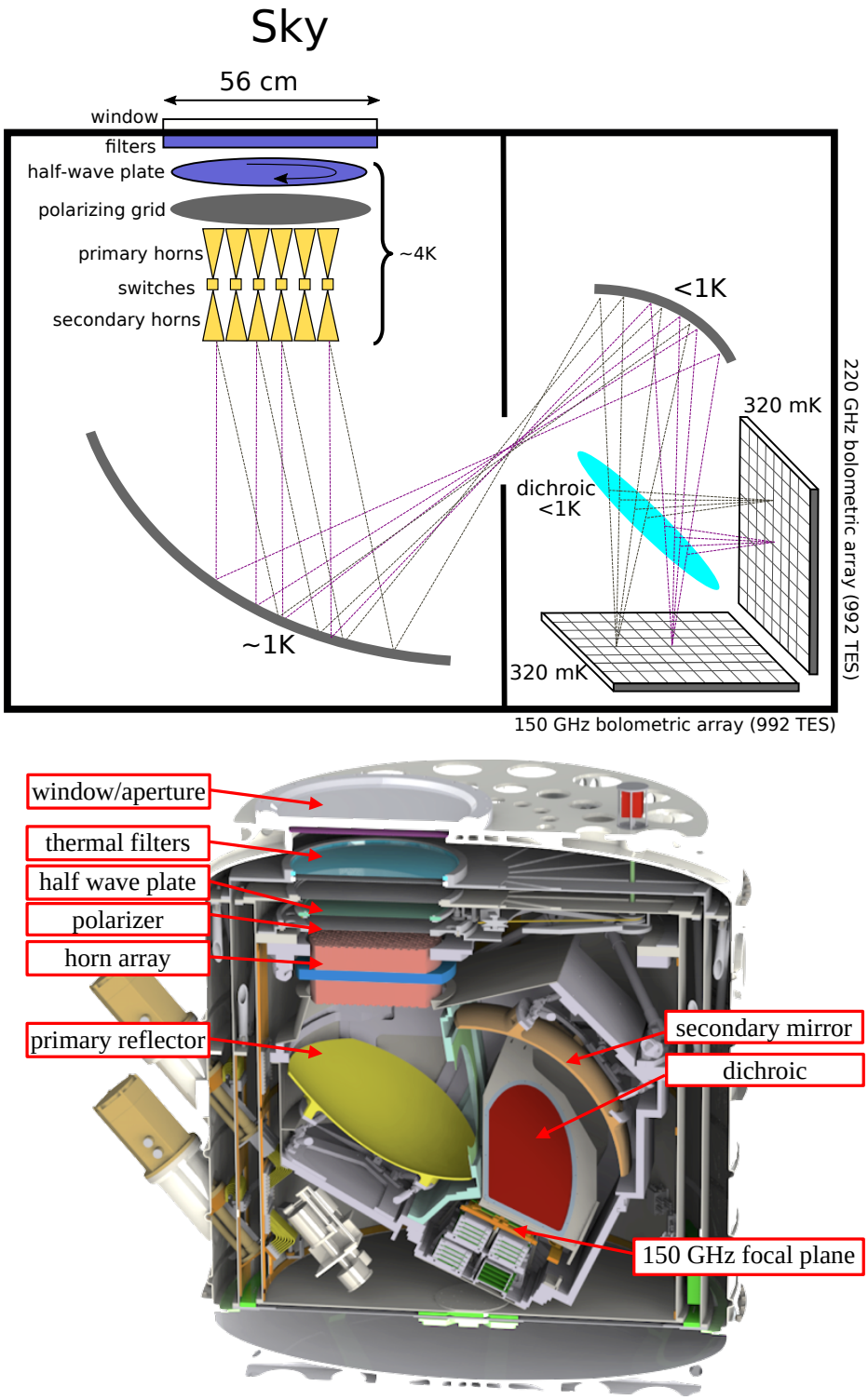

Figure 1. Schematic of the QUBIC-FI instrument (above) and sectional cut of the cryostat (below) showing the same sub-systems in their real configuration. The second detector array is not shown in the CAD rendered image below.

JCAP04(2022)036

Parameter	QUBIC-TD	QUBIC-FI
Frequency channels	150 GHz	150 GHz & 220 GHz
Frequency range 150 GHz	[131–169] GHz	[131–169] GHz
Frequency range 220 GHz	—	[192.5–247.5] GHz
Window Aperture [m]	0.56	0.56
Number of horns	64	400
Number of detectors	248	992×2
Detector noise [$W/\sqrt{Hz}$]	2.05×10^{-16}	4.7×10^{-17}
Focal plane temp. [mK]	300	300
Sky Coverage	1.5%	1.5%
Synthesized beam FWHM [degrees]	0.68	0.39 (150 GHz), 0.27 (220 GHz)

Table 1. QUBIC main parameters

only in the number of horns and detectors, and it lacks the dichroic and second focal plane for 220 GHz. The sky signal first goes through a 56 cm diameter window made of ultra high molecular weight polyethylene followed by a series of low-pass filters cutting off frequencies outside the desired band. The window is not anti-reflection coated. The filters are Cardiff metal mesh filters (see O'Sullivan et al. [7] for details).

The next optical component is the stepped rotating HWP which modulates incoming polarization (see D'Alessandro et al. [13] for details). The HWP is a metal-mesh device as described by Pisano et al. [14]. A single linear polarization is selected just after polarization modulation by a wire-grid. In this scheme, any unwanted cross-polarization which might be introduced by components later in the optical chain do not affect the result since the bolometers absorb all radiation, independent of polarization.

The next optical device in the QUBIC-FI is an array of 400 back-to-back corrugated horns made of an assembly of two 400-horn arrays, composed of 175 aluminium platelets (0.3 mm thick) chemically etched to reproduce the corrugations required for the horns to achieve the required performance. The horn mouth diameter is 12 mm and the spacing between horn centres on a row is 14 mm. For the QUBIC-TD, there are only 64 horns. Both front and back horns are identical with a field of view of 13 degrees FWHM with secondary lobes below −25 dB [15]. An array of mechanical shutters (RF switches) separates the two back-to-back horn arrays in order to be able to close or open horns for self-calibration (see section 4.3). The shutters are spring loaded and activated by applying a voltage to an induction coil. As a result, the shutter requires continuous electrical current in order to remain closed. This dissipates some heat such that it is only possible to activate a maximum of two shutters at a time without over heating the horn array which is maintained at 1 K.

The back-horns directly illuminate the two-mirror off-axis Gregorian optical combiner [7] which focuses the signal onto the two perpendicular focal planes in the QUBIC-FI and only one focal plane in the QUBIC-TD. In the QUBIC-FI, a dichroic filter splits the incoming waves into two wide bands centred at 150 GHz for the on-axis focal plane and 220 GHz for the off-axis focal plane. The QUBIC-FI focal planes are each equipped with 992 NbSi TES [9] cooled to 320 mK using a double-stage ^{3}He/^{4}He sorption cooler [8]. The QUBIC-TD has only 248 TES.

A schematic view and CAD model of the cryostat can be seen in figure 1. The cryostat weighs roughly 800 kg and is around 1.6 m high with a 1.4 m diameter. The QUBIC-TD

JCAP04(2022)036

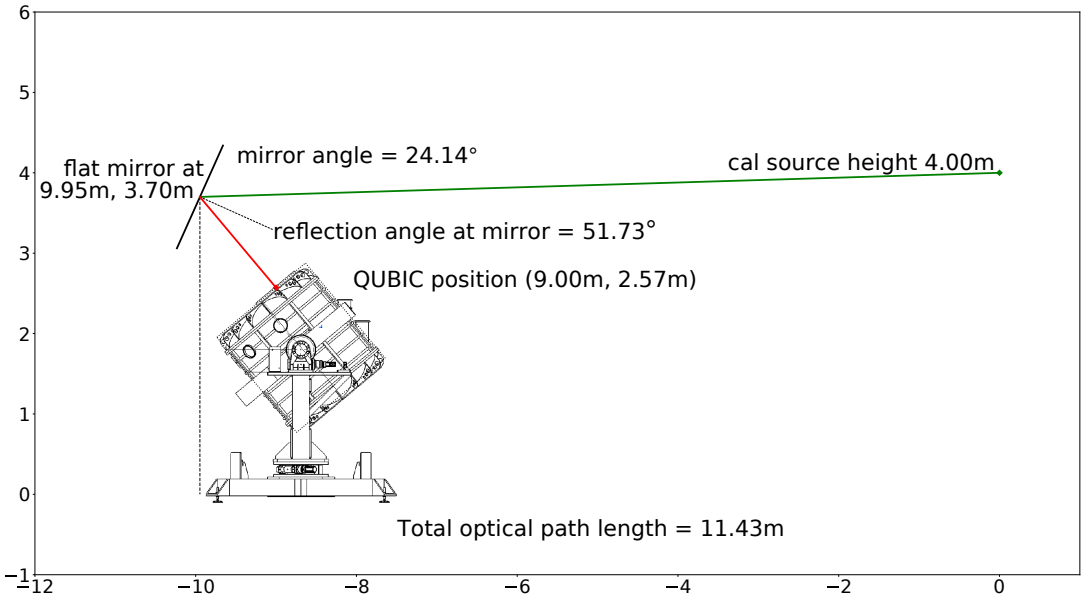

Figure 2. Layout for the calibration source relative to the QUBIC instrument.

includes all the critical elements of the QUBIC-FI, thus making the test campaign presented here representative of the complete configuration. The QUBIC-TD uses the same cryostat, cooling system, filters and general sub-system architecture as the QUBIC-FI but with only 64 back-to-back horns and smaller mirrors to match the illumination of the 8×8 horn-array. It has a single 248 TES bolometer array operating at 150 GHz. The QUBIC-FI will have improved performance because of the increased size of the horn cluster and the increased number of detectors, as explained in section 1. Also, the QUBIC-FI detectors will be background-limited. The QUBIC-TD detection chain is currently not background-limited because of aliasing in the readout system [9]. The QUBIC-FI will have increased sampling frequency and will add Nyquist inductors to mitigate this effect.

Throughout this paper, we use our in-house Python-based software called `qubicsoft`[1] for data analysis, and for hardware control and monitoring. The `qubicsoft` package is also used for data simulations, except where otherwise indicated.

3 Calibration source

3.1 Setup for QUBIC-TD

Characterization of the QUBIC-TD instrument is done primarily using a frequency-tunable monochromatic point source in the far-field. This permits measurement of the bandpass (section 4.1), the polarization performance (section 4.2), the measurement of interference fringes (section 4.3), and the beam point spread function (PSF, section 4.4 and section 4.5). This section describes the optical setup used to characterize QUBIC-TD.

The setup is shown in the sketch of figure 2. The calibration source points at a flat mirror which redirects the beam into the QUBIC cryostat window. There is an 11 m optical path putting the calibration source effectively in the far field (see section 3.2).

[1] https://github.com/qubicsoft.

JCAP04(2022)036

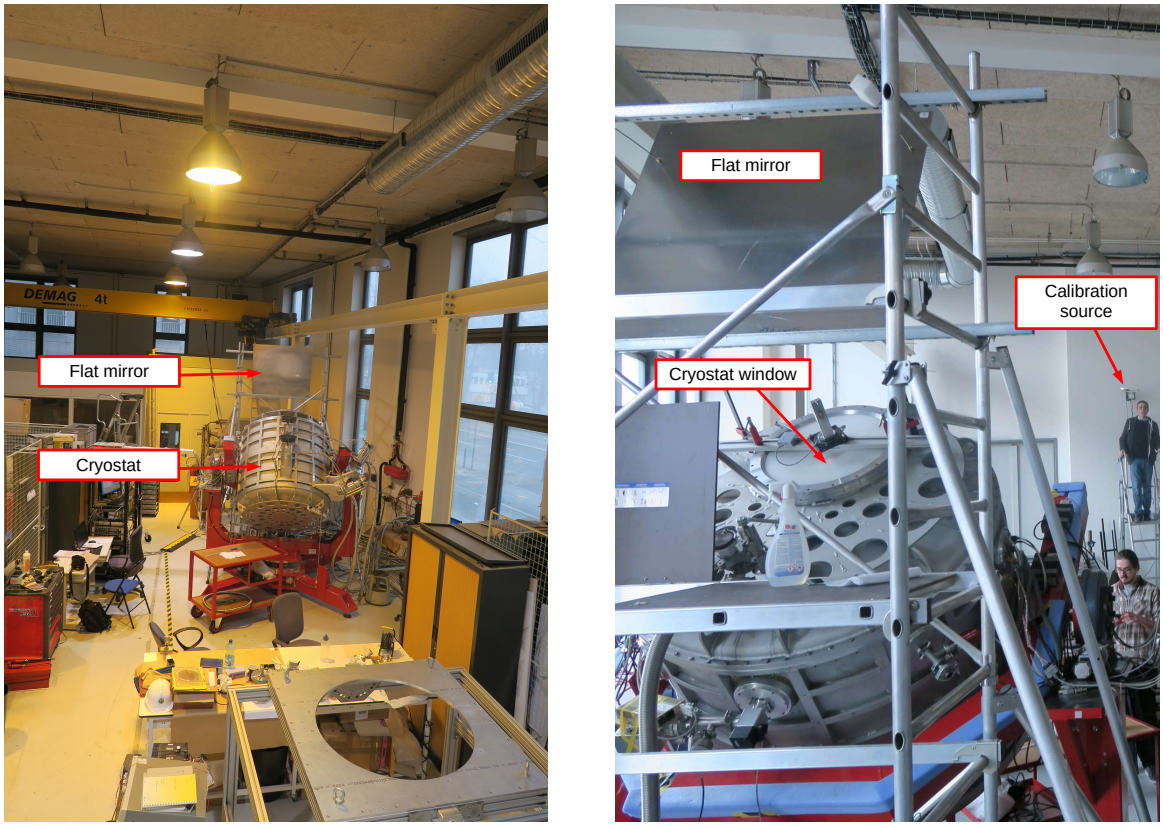

Figure 3. *Left:* photo of QUBIC looking along the line-of-sight from the calibration source. The reflection of the window is clearly visible in the flat mirror. *Right:* the flat mirror is mounted on a scaffold at a height of 3.7 m and has a finely adjustable tilt angle using a system composed of a long screw.

The flat mirror is an aluminium sheet mounted on a scaffolding at a height of 3.7 m (photo in figure 3). The tilt angle of the flat mirror can be adjusted by a long screw ensuring precise selection for the correct tilt angle.

Alignment of the system was accomplished using a laser temporarily mounted at the window of the QUBIC cryostat, pointing normal to the window (photo figure 4). The laser light is reflected from the flat mirror to the calibration source where a small flat mirror was fitted to the front of the calibration source feedhorn. The laser reflects from the mirror at the feedhorn mouth and returns to the large flat mirror and finally to the QUBIC cryostat window. In the photo (figure 4), one can clearly see the spot of the laser on the corner of the laser mounting structure on the window. The alignment is therefore precise to within a fraction of a degree which is well within the tolerance necessary to have the calibration source visible to the QUBIC-TD.

The calibration source system is composed by the source itself together with a dedicated electronic subsystem supporting its operations. The calibration source was purchased from Virginia Diodes Incorporated (VDI) electronics[2] and is composed of a synthesizer providing frequencies around 10 GHz followed by a two-stage multiplication chain. A coaxial cable from the synthesizer connected by standard SMA connectors leads to the first of two multipliers

[2] https://vadiodes.com.

JCAP04(2022)036

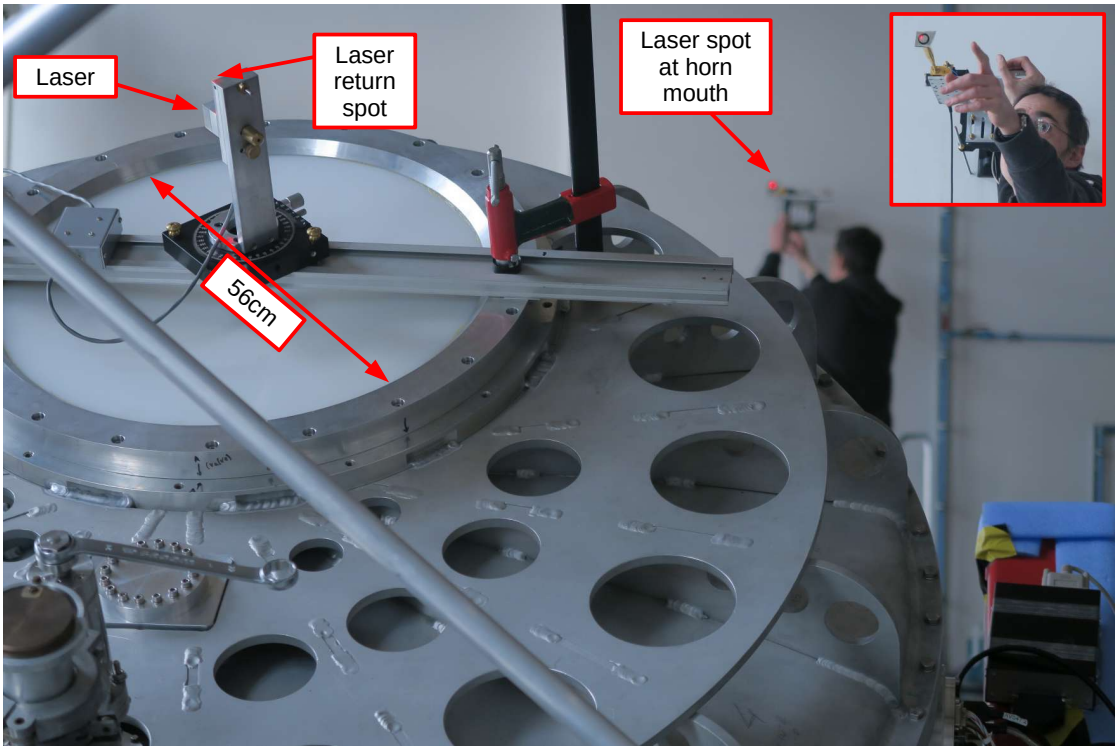

Figure 4. Photo of the alignment procedure. The laser is mounted orthogonal to the cryostat window and shines towards the flat mirror, sending the light to the calibration source feedhorn at the other side of the room. A small mirror fitted to the mouth of the feedhorn sends the laser light back on the same path to the cryostat window. The laser spot is clearly visible on the laser mount structure. The inset, top-right, shows a close-up of the calibration source with a mirror mounted on the horn mouth and the laser spot within the area of the horn mouth.

which are in a waveguide-coupled chain. Together, they multiply the base frequency by 12 resulting in frequencies around 150 GHz. The signal is transmitted by rectangular waveguide after the final multiplier to a profiled corrugated feedhorn. The range of the system is between 130 GHz and 170 GHz with a frequency tuning resolution of 144 Hz. The nominal output power is +9 dBm and it can be modulated with a maximum amplitude of 1.25 dB. The frequency is configured via USB connection by a nearby Raspberry Pi mini computer (see photo figure 5).

A signal generator provides a square wave at around 1 Hz which is used to modulate the amplitude of the calibration source. The Raspberry Pi configures the signal generator, selecting the amplitude, offset, frequency, shape, and duty cycle. A directional coupler at the waveguide before the entrance to the corrugated feedhorn provides a port for monitoring the output power of the calibration source. The horn return loss is less than −30 dB, as reported by the supplier of the horn, Custom Microwaves Inc.,[3] and therefore the monitoring of the output power variation at the end of the multiplier chain is a reliable method for monitoring the power variation in the calibration source output power illuminating the aperture of QUBIC-TD. A probe on this port provides a voltage which is a function of the output power. This voltage is sent to an analogue-to-digital converter (ADC) board integrated in the

[3] https://custommicrowave.com.

JCAP04(2022)036

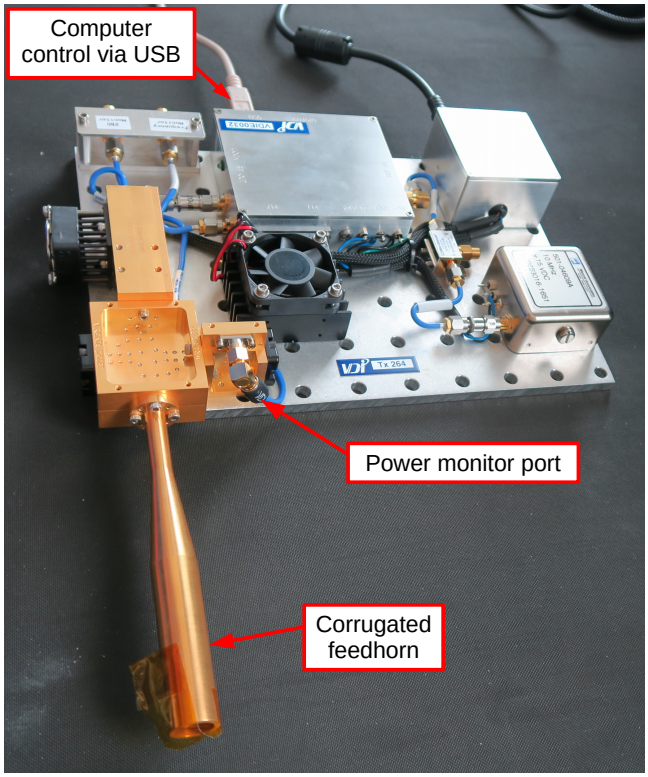

Figure 5. Photo of the VDI millimetre-wave source. The electronics include a signal generator for modulating the calibration source with a square wave. The output power monitor of the calibration source is sent through an amplifier and then digitized by an ADC board integrated in the Raspberry Pi (seen suspended on the cables below the calibration source).

Raspberry Pi mini computer which broadcasts the data on the internel network along with a timestamp for each sample. There are approximately 300 samples per second. A command line interface written in Python is used to configure the calibration source setup. This system accepts commands via network socket and can be easily interfaced by the graphical user interface called `QubicStudio`.

There is an important difference in the background loading for the QUBIC-TD in the lab compared to an on-sky measurement. The lab background loading is of the order of 300 K, while a measurement on the sky will have background loading of the order of a few tens of K. In order to reduce the laboratory background loading, the QUBIC-TD is equipped with a neutral density filter (NDF) mounted at the 1 K stage. The NDF transmits 9% of all incoming radiation. This reduces the 300 K ambient temperature background to about 27 K which approximates what is expected from the sky at the 5000 m above sea-level observing site. As a result, the loading on the bolometers in the laboratory measurements with the NDF approximates what it will be at the observing site without the NDF.

A second difference between the setup in the lab and the planned setup for the instrument at its observing site is the power received by the calibration source. The VDI millimetre-wave source emits significant power. In the laboratory setup, it is placed at a distance of 11.4 m, while at the observing site, the calibration source will be mounted on a tower 40 m distant from the base of the QUBIC telescope, giving an optical path length of approximately 60 m. This means that the calibration source detected in the lab is roughly 30 times more powerful than

JCAP04(2022)036

in the setup planned at the observing site. For this reason, Eccosorb material AN72 is placed at the calibration source feedhorn mouth in order to attenuate the signal to approximately 3% across the band (see Schillaci et al. [16] for a measurement of attenuation by Eccosorb).

Figure 6 shows the signal response of all the TES detectors in the QUBIC-TD array. The source was set at 150 GHz and was modulated with a square wave with 3 second period (0.333 Hz) and a 33% duty cycle. The period was chosen to be significantly longer than the expected time constant of the TES bolometers, and with a non-symmetrical duty cycle $(1/3, 2/3)$ in order to easily distinguish the OFF and ON cycles. Figure 7 shows in detail the signal measured by a typical well-behaved TES together with the modulation signal measured by the power monitor. There is a clear correlation between the two and the time constant can be estimated to be of the order of 40 ms. A detailed analysis of the QUBIC-TD bolometer response is given in Piat et al. [9].

While the APC laboratory is not equipped as an anechoic environment (see figure 3), our measurements show no evidence of reflection effects from the surroundings. The mapping of the beam did not show unwanted artefacts (see, e.g., figure 16 in section 4.4, and also the result of the mapmaking algorithm, figure 18, in section 4.5). Nevertheless, it is possible that low-level reflections may have contributed some extra noise to the image. The diffuse features around the peaks may be due to reflections in the lab, or they are possibly due to instrumental imperfections that can be dealt with at the map-making stage once they are measured. These maps are expected to be improved when the measurements are made at the observing site where external reflections will be at a much lower level, while instrumental artefacts remain the same.

Another possibility for reflections might come from the face-to-face setup of the calibration source and the QUBIC window. This could lead to standing-waves but a number of parameters mitigate this possibility. The long optical path between the cryostat window and the calibration source imposes significant attenuation of the signal after reflection, and multiple reflections will have insignificant power. The mouth of the feedhorn at the calibration source subtends an angle of approximately 0.05 degrees, therefore exposing negligible area to the cryostat window for reflections. Finally, a layer of Eccosorb AN72 was placed in front of the calibration source feedhorn mouth for further attenuation. If we use purely geometric optics reasoning, which gives an upper limit to the magnitude of standing waves, we can simply compare the area of the two face-to-face surfaces. The QUBIC-TD window has a diameter of 56 cm and the calibration source feedhorn has a diameter of 1 cm. The ratio of the areas of these surfaces is less than 0.03%. Therefore the power is attenuated by 0.03%, without considering the attenuation by the Eccosorb and by the distance between the two surfaces. This is below our measurement precision. For example, the bandpass measurement of figure 10 in section 4.1 shows no evidence of standing waves.

3.2 Optical modelling of the calibration source as viewed by QUBIC

For an accurate analysis of the instrument performance, it is important to have a simulation of the expected pattern on the focal plane. For this purpose, we use optical modelling with the source set at the same distance (11.4 m from the QUBIC-TD window) as in our experimental setup. The comparison between measurement and model is done regardless of the distance to the calibration source, however it is also useful to have the calibration source sufficiently in the far-field so that it appears as an unresolved point source resulting in the focal plane pattern being the PSF of the instrument. The PSF has several sharp features with which to

JCAP04(2022)036

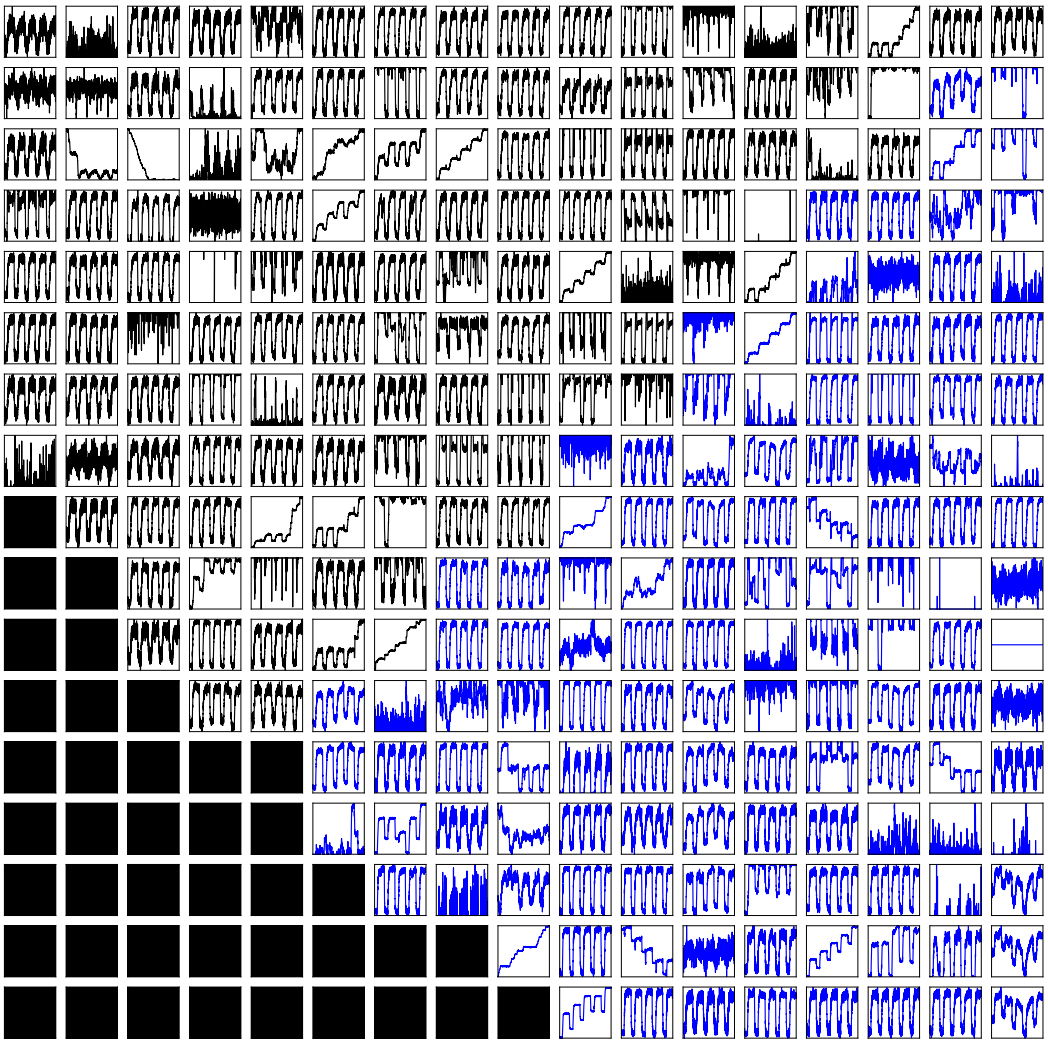

Figure 6. The first measurement of the calibration source by QUBIC. Each box in the plot shows a 20 second timeline for the detector in that position in the focal plane. The vertical axis for each plot is in arbitrary power units, scaled for the minimum and maximum of each plot. The signal is clearly seen in most pixels, corresponding to the good pixels in the array (see Piat et al. [9] for a discussion on the bolometer array performance). The curves in blue and black differentiate the two read-out electronics chains (128 detectors per read-out electronics box). The black, filled-in "pixels" in the bottom-left are empty positions. The QUBIC-FI will have four arrays equivalent to this one in order to make a roughly circular focal plane for each frequency channel.

compare. Once in the far-field the focal plane pattern does not vary significantly with the distance to the calibrator.

Using the software package `MODAL` (Maynooth University, see O'Sullivan et al. [7] for details about optics modelling), a model of the 150 GHz source was positioned 1 m and 10 m from the aperture. For each position the following quantities were determined:

- the incident radiation over the horn array.
- the horn output (at a distance of 60 cm) for two arbitrarily chosen horns in the 8×8 horn array.

JCAP04(2022)036

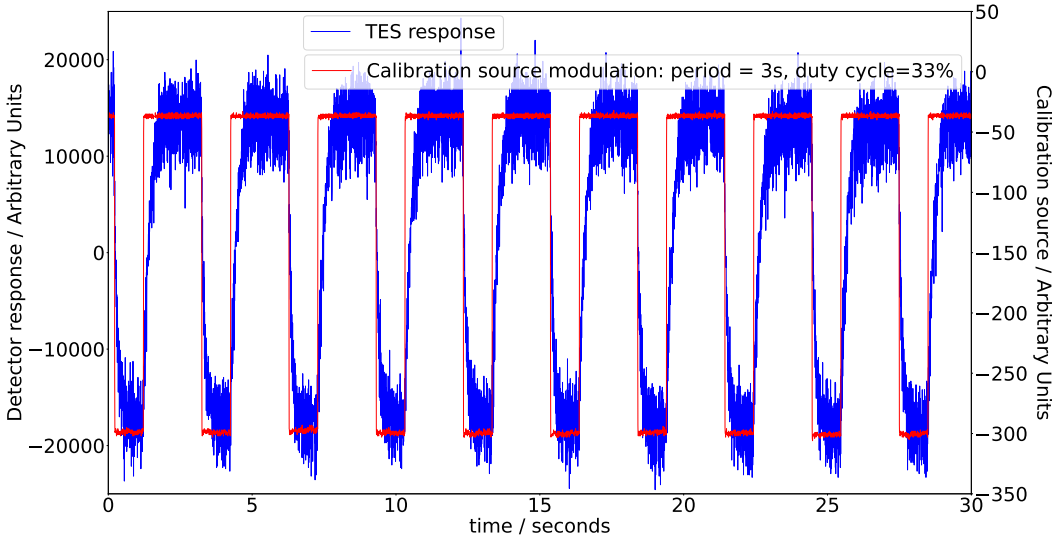

Figure 7. Overlay of the signal detected by a TES detector of the QUBIC array (blue curve) together with the modulated calibration source signal as measured by the calibration source power monitor (red curve).

- the resulting PSF on the focal plane formed from the radiation for all 64 horns in the array.

Both the amplitude and phase of the incident field from the calibrator source were investigated at the input of the horn array. It can be seen in figure 8 that at a distance of 10 m, the amplitude and phase of the calibrator beam is quite uniform over the horn array.

Investigating the output of different horns in the array provides another insight into the coupling to the incident source radiation. Incident radiation couples with the horn and excites it, causing it to emit a beam which is approximately a 12.9° Gaussian beam in the far-field. For an on-axis source in the far-field of the instrument, the radiation over the array is uniform and the coupling the same for all of the horns, meaning that all the horns will emit a Gaussian-like beam of the same amplitude and the same phase. If the incident radiation is not uniform over the array, as is the case for the source at 1 m, then it will not couple to the horns in the same way and the horn output will be different. When the source is farther away, the coupling across the array becomes more uniform. All of the horn beams have the same profile. The difference in coupling can be seen as the difference in the peak intensity. With the calibration source at 10 m distance, the beams from the two sample horns are similar.

The PSF calculated for some of the calibrator source distances investigated are shown in figure 9 [17]. With the source placed 1 m from the array, the image on the focal plane has more relative power spread throughout the image and a less clearly visible cross-like structure compared to the image with the source further away. A source distance of 10 m shows a pattern that resembles the expected PSF figure 9 (middle). This implies that the source distance of 11.4 m is sufficiently faraway for the calibrator to be used to measure the PSF of the TD. An optical path of 11.4 m was achieved by placing the source on a lab wall and using a mirror to reflect it into the QUBIC-TD aperture.

JCAP04(2022)036

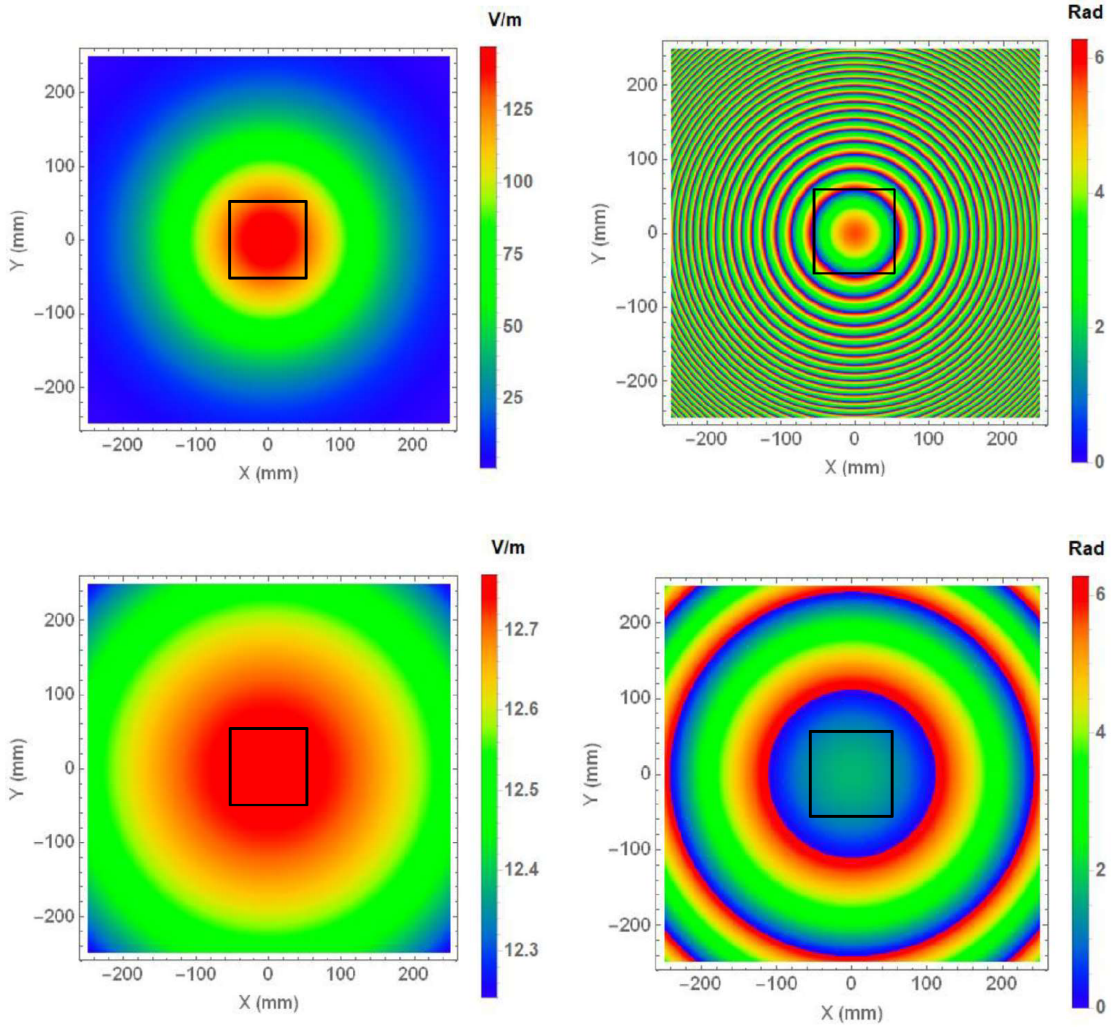

Figure 8. Simulated beam pattern amplitude (left) and phase (right) from the source over the horn array of QUBIC when the calibrator source is placed 1 m (top) and 10 m (bottom) from the aperture, with the position and size of the horn array shown in black.

JCAP04(2022)036

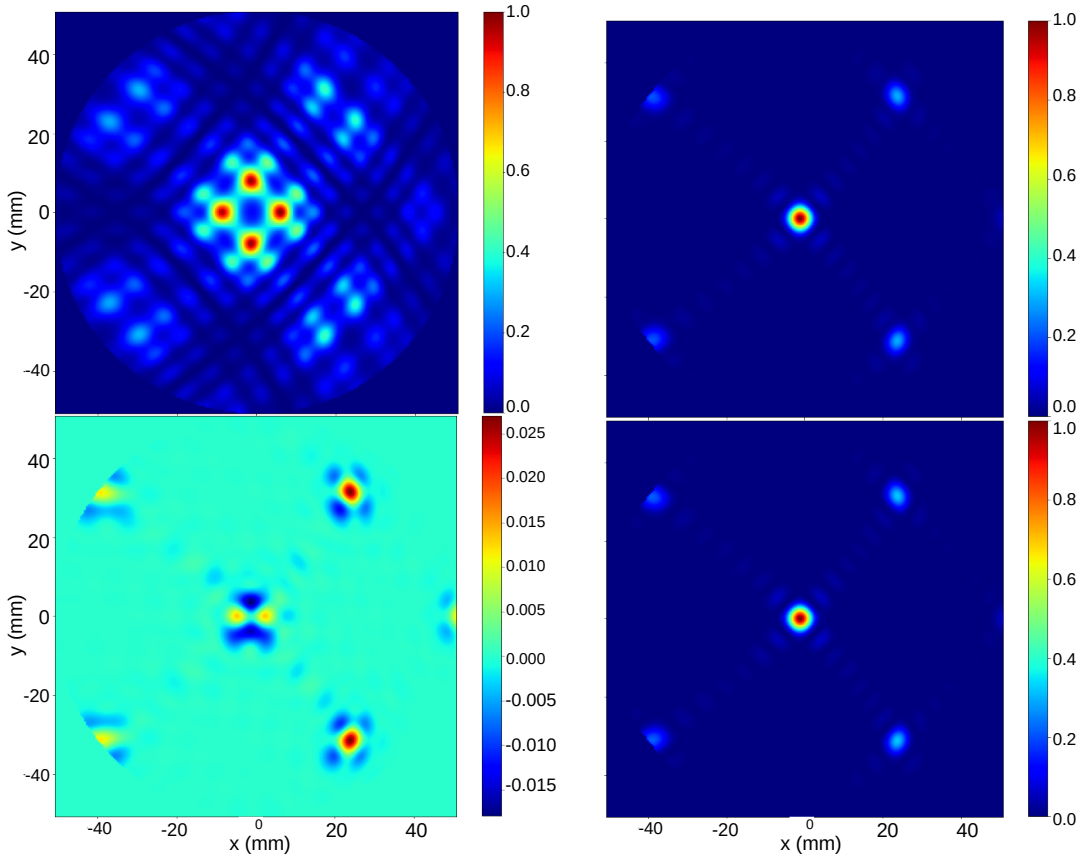

Figure 9. Simulated intensity of the interference pattern on the QUBIC focal plane when observing the calibration source at various distances from the instrument aperture. Clockwise from top-left: source at 1 m, source at 11.4 m, source at infinite distance, difference between the source at 11.4 m and at infinity. The colour bar gives the normalized intensity at each distance. The peak residual is 0.025.

JCAP04(2022)036

4 Measurement results and analysis

4.1 Spectral response

The spectral response was measured using the calibration source (see section 3). The calibration source was modulated with a 1 Hz sine wave modulation and was stepped through frequencies across the band from 120 GHz to 180 GHz, taking 60 seconds of data at each frequency setting. The calibration source output power was measured independently by a zero-bias detector at the output of the amplitude multiplication chain, as described in section 3. Synchronized demodulation of the calibration source output and the bolometer response provides a high signal-to-noise measurement which also accounts for any spectral variation in the calibration source output power. Figure 10 shows the measured profile. The error bars are statistical and calculated from the uncertainty in the demodulation of the calibration source signal. The spectral response is flat to within 1.5 dB inside the range 136 GHz to 173 GHz, and drops by ~ 2.5 dB at the nominal band edge of 130 GHz.

The calibration source is designed to operate between 130 and 170 GHz (shown as the white region bordered by vertical dashed lines in figure 10). Its use below and above these limits was not characterized by the supplier, Virginia Diodes Incorporated (VDI) and it should not be used to make quantitative conclusions due to uncertainty in the tuning frequency and in the level of the output power outside the designed spectral range. Nevertheless, we operated the calibration source outside its nominal range, to obtain a qualitative behaviour of the spectral response of the intrument below and above the desired frequency range. We also placed a layer of Eccosorb material AN72 at the mouth of the calibration source corrugated feedhorn in order to attenuate the high power output of the source. This provides 25 dB of attenuation with a spectrally flat profile ($\pm 1\%$ across the band), as measured by a vector network analyser at the laboratory of the University of Milan.

The QUBIC-TD optical path includes 13 multi-mesh blocking filters manufactured by QMC Instruments Ltd – Thomas Keating Instruments Ltd[4]. These are particularly important in the laboratory environment which has a background thermal loading at room temperature, in contrast to what will be the situation for the instrument when it is on the observing site and pointing at the sky with a background thermal loading on the order of 10 K. The 13 filters are distributed along the optical path inside the cryostat and are heat sunk to the different temperature stages between 300 K and 0.3 K. For more details on the optical design see O'Sullivan et al. [7] and for the cryogenic design, see Masi et al. [8]. In order to further attenuate the 300 K environment in the laboratory, the QUBIC-TD has a neutral density filter which is a thermally evaporated gold layer on a 1.5 μm mylar substrate. It was tested to give a 9% transmission at room temperature. The combined filter profile is shown as a brown-dashed curve in figure 10 and includes all the filters in the optical train as well as the horn waveguide cut-off profile. The back-to-back horn array has a waveguide "throat" section with a diameter that creates a low-frequency cut-off at 125 GHz. Details of the horn array are described in Cavaliere et al. [15].

The measured spectral profile differs from the expected profile at the band edges with additional suppression at the low frequency end, and additional transmission at the high frequency end. The difference is ~ 2.5 dB excess suppression at 130 GHz and ~ 4.5 dB at 173 GHz. The differences will be investigated in future measurements, however, this does not have a significant effect on the overall performance of the QUBIC-TD. In particular, the

[4] http://www.terahertz.co.uk/.

JCAP04(2022)036

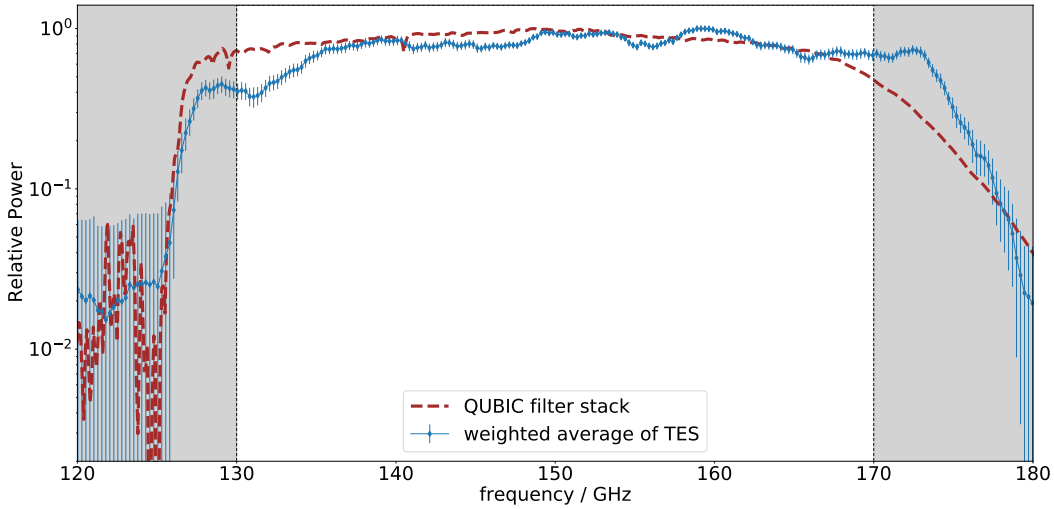

Figure 10. Bandpass of the QUBIC-TD. This was measured by stepping through the frequencies of the calibration source and measuring the relative power on the TES at each frequency. The expected profile from the combined effect of filters and the horn array is shown as the brown-dashed curve. Note that the calibration source performance is uncertain outside the band 130 GHz to 170 GHz (area shown in grey, and see main text).

measured bandpass falls well within the atmospheric window between the 119 GHz oxygen line and the 183 GHz water line.

4.2 Half wave plate polarization rotation test

A functionality test of the HWP rotator mechanism was carried out while, at the same time, the calibration source was operating. The calibration source, composed of a rectangular waveguide and a corrugated horn, is linear polarized with cross-polarization less than −30 dB, as quoted by the supplier of the corrugated horn, Custom Microwaves Inc.[5] Measurements were taken at each of the 7 evenly spaced positions of the HWP from 0° to 90° (spacing of 15°). Figure 11 shows the signal for a TES near the centre of the focal plane at different HWP orientations (shown in different colours). The peak-to-peak amplitude clearly shows repeatable variations with HWP position. The HWP orientation in position #3 rotates the calibration source polarization such that it is orthogonal to the polarizing grid (see figure 1 and section 2). Figure 12 shows a subset of 4 seconds of the calibration source signal measured by a TES near the centre of the focal plane with the HWP in position #1 and in position #3. There are 180 seconds of data at each of the 7 HWP positions, giving high signal-to-noise and the small error bars seen in figure 13.

The amplitude at each position is plotted and fitted to a sine curve, with the amplitude normalized, as shown in figure 13. The signal in each case is measured by the RMS of the TES data while the source was modulated. The measurement is the source modulation amplitude together with the RMS of the noise, quadratically added. As a result the minimum value is dominated by noise. The maximum signal occurs when the HWP is between position 6 and 7. This measurement represents a direct measurement of the cross-polarization response of the QUBIC-TD. The cross-polarization contamination at 150 GHz for the TES near the centre of the focal plane is compatible with zero to within 0.4% at 95% confidence level. We

[5] https://custommicrowave.com/.

JCAP04(2022)036

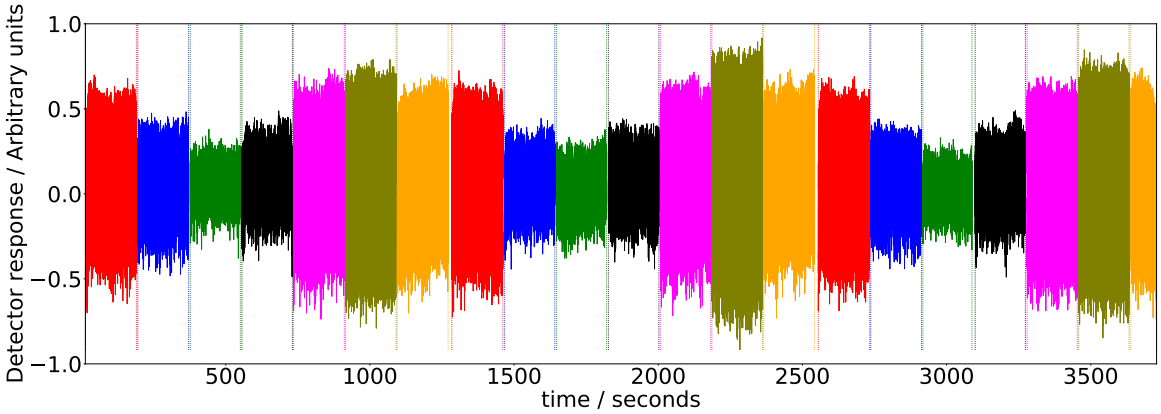

Figure 11. Peak-to-peak amplitude of the detected calibration source for different HWP positions as measured with a TES near the centre of the focal plane. The 7 positions are spaced by 15° in order to span 90° between position 1 and position 7.

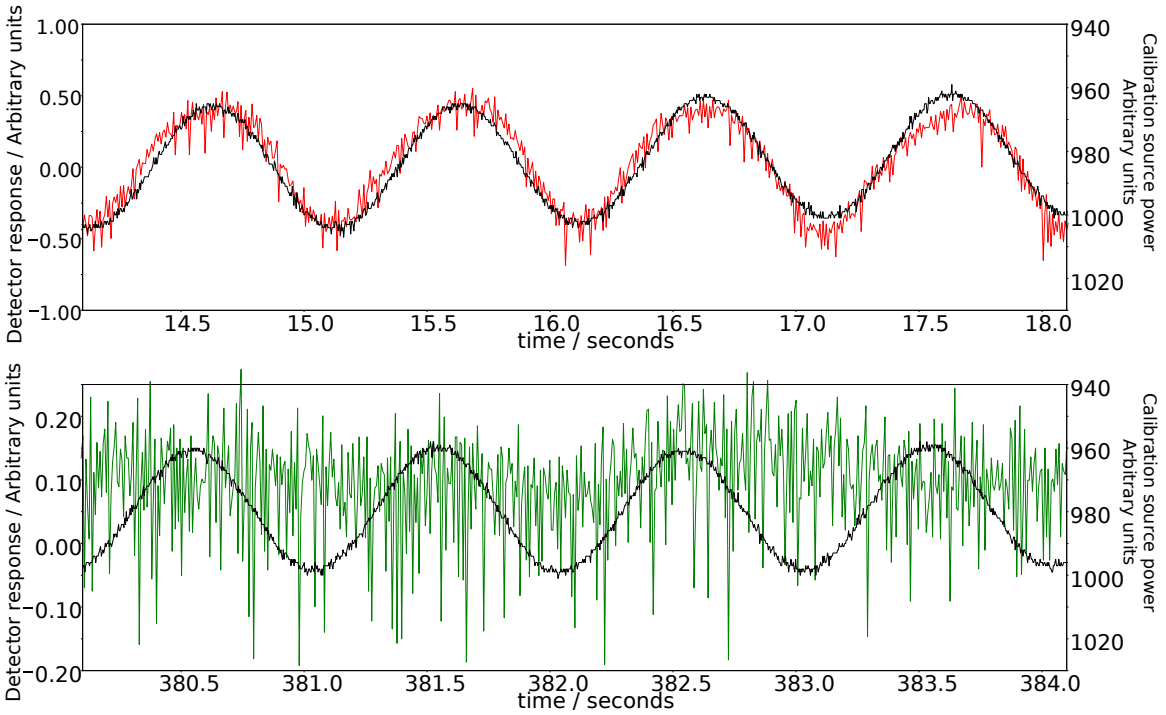

Figure 12. Close-up view of the peak-to-peak amplitude of the detected calibration source for the HWP in position #1 (top) and position #3 (bottom) as measured with a TES near the centre of the focal plane. The black curve is the power of the calibration source as measured by the power monitor (see section 3). It is plotted over the measured response of the bolometer (top, red curve for position #1 and bottom, green curve for position #3). The HWP in position #3 rotates the incoming calibration source polarization such that it is orthogonal to the polarizing grid. This is seen in the low level of modulation in the signal.

JCAP04(2022)036

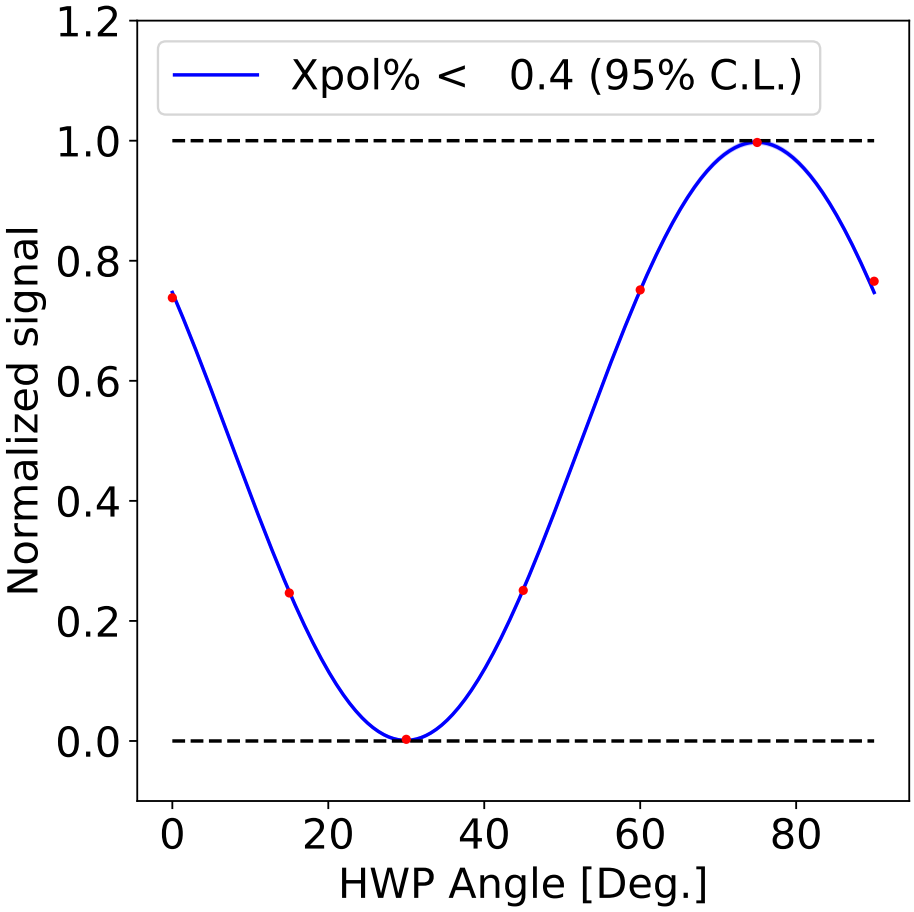

Figure 13. Amplitude of the detected calibration source at 150 GHz as measured with a TES near the centre of the focal plane for the HWP in the different positions and fitted to a sine curve.

use the definition of cross-polarization described by eq. 1 of Ludwig [18]. The full analysis for all working detectors in the focal plane gives a median value of 0.61% at 95% confidence level [13].

The calibration source can be modulated with a choice of modulation frequency, amplitude, and total power output (see section 2). The power offset and amplitude can lead to saturation of the TES detectors, as shown in figure 14. The detector in this case is saturated at HWP positions which rotate the calibration source polarization closer to co-aligned with the polarizing grid. The amplitude plotted in figure 14 is the normalized amplitude such that the HWP rotation curve fits a sine curve with peak-to-peak amplitude of 1. A sine curve fitting the lower part of the curve but not the upper part of the curve is an indication of saturation. Figure 14 is used to determine optimal calibration source settings so that the detector is not saturated at any HWP position. Saturation is calculated using the saturation parameter as described in D'Alessandro et al. [13] (eq. 9.2). For the TES in figure 13 the saturation level is less than 0.23%.

As polarization is selected before the horn array (see section 2), the cross-polarization leakage is independent of the location in the focal plane. Therefore, the cross-polarization leakage is expected to be the same for all TES. The example shown in figures 13 and 14

JCAP04(2022)036

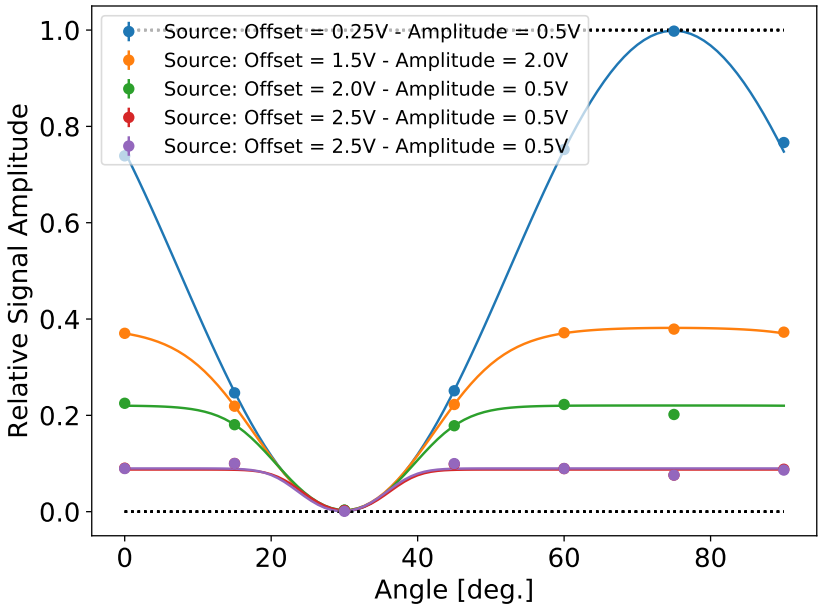

Figure 14. Same as figure 13 but with the calibration source set at various power output levels. The effect of saturation is evident for the source at high power. The HWP angle of maximum signal damping is consistent between all the measurements.

are for a TES near the centre of the focal plane which has the best signal-to-noise for this measurement due to the pointing.

The cross-polarization contamination was measured with the calibration source tuned to 150 GHz. This is therefore a measurement at a single, essentially monochromatic frequency. Future test campaigns will measure the cross-polarization contamination at frequencies across the band in order to determine the integrated response of the system for the full bandpass.

4.3 Self-calibration and the measurement of fringes

Self-calibration is a technique developed for aperture synthesis in radio interferometry. This technique evolved from the original idea in the 1970's of "phase-closure" [19–21] to become in the early 1980's "self-calibration" [22, 23]. See Cornwell & Fomalont [24] for a detailed overview. Precise knowledge of the calibration source is not required, as long as it is a strong and stable point source. The large number of baseline visibilities allows us to solve for many unknowns, including the gain and phase corrections of each detector, without requiring knowledge of the source amplitude.

In order to advance towards the full analysis of self-calibration, a key component is the ability to measure fringes with QUBIC. If fringes can be measured with a horn pair, then the full analysis can be done once the fringe measurement is done for all horn pairs. By measuring the fringe pattern of a single pair of horns we demonstrate the feasibility of doing self-calibration with the bolometric interferometer.

The QUBIC-TD successfully measured fringes between a pair of horns (figure 15 left). The measured fringe pattern in figure 15 (left) is the interference pattern of one baseline which corresponds to a set of two horns. It is the derived image after analysing measurements of images with all horns open, with two horns closed, with one horn closed, and with the other horn closed. This measurement takes approximately 30 minutes, cycling through the switch

JCAP04(2022)036

configurations (horn 'a' open, horn 'b' open; horn 'a' closed, horn 'b' open; horn 'a' closed, horn 'b' closed; horn 'a' open, horn 'b' closed). Each configuration is measured for 20 seconds, and the timeline is co-added (folded by the cycle period). The result is the equivalent of having all horns closed except the two of interest, as was shown in Bigot-Sazy et al. [10]. It is necessary to make the measurement in this way because of the limitation required on heat dissipation. Only a maximum of two switches can be activated (closed) at a time, as described in section 2 (and see Cavaliere et al. [15] for full details). As a result, it is not possible to close all horn switches except for the two of interest. However, using the analysis steps described above, figure 15 (left) is the result of interference between a single pair of horns.

The fringes are expected to be fainter in proportion to the distance to the centre of the focal plane (figure 15 right). This is not the case here because of saturation of the TES detectors. As a result, the fringe amplitude appears to be relatively constant, or near zero where saturated detectors were subtracted from one another. The problem with saturation is mainly related to the high power of the calibration source. The calibration source can be attenuated by its bias voltage, which is used for signal modulation (see, for example, figure 14 in section 4.2). It can also be attenuated by moving the HWP, as seen in figure 13 of section 4.2. Future tests will explore methods to attenuate the calibration source while still having enough signal-to-noise to measure the secondary lobes of the synthesized beam.

It is worth noting that the difficulty with saturation of TES is more problematic for the analysis of fringes than for the analysis of the HWP presented in section 4.2. This is because the HWP measurements were done with a single TES at a time. This allows us to test the HWP performance with optimal settings on a given TES, and thus separate the HWP performance from the TES performance. The fringe measurement requires constructing an image on the focal plane, and this necessitates the use of multiple TES. The TES manufacturing is not perfectly homogenous (see Piat et al. [9] for details) and the optimum bias settings vary somewhat from TES to TES. The electronics supplying the bias settings for the TES can only supply the same bias to all 128 TES configured by each ASIC. As a result, some of the TES are not optimally biassed, and saturation could be a problem for some while not for others. A solution to the problem is to make a sky map of the fringes, in the same way we made the map of the synthesized beam. In order to do this, a map must be made for each horn-switch configuration (single horns open/closed and pairs open/closed). This will be time consuming, but it is done with the artificial calibration source, and so can be done during times when QUBIC is not measuring the sky. Eventually, we will build a data base of maps with all the horn configurations.

4.4 Synthesized full beam reconstruction

The QUBIC-TD synthesized beam maps were measured at five frequencies in the range 130 GHz to 170 GHz by tuning the VDI calibration source (see section 3) in steps of 10 GHz from 130 GHz. For each frequency measurement the calibration source was modulated at a period of 1 second with a sinusoidal profile, and the TES signal was demodulated in post processing. QUBIC-TD was configured to point at an elevation angle of 35° and to scan across azimuth at a constant rate from −25° to +25°. The elevation angle was then increased by 0.2° and a new azimuth scan at constant rate was done in the reverse direction from +25° to −25°. Each azimuth scan takes nearly 8 minutes, and an entire beam map at a given frequency is completed in 22 hours and 30 minutes. This matches well with the cryogenic hold time of the cryostat. The entire beam map measurement was preprogrammed in a script executed by the QUBIC instrument control software `QubicStudio`.

JCAP04(2022)036

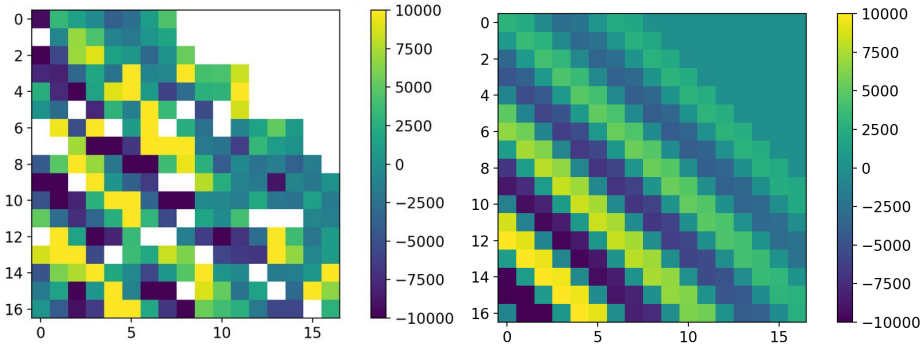

Figure 15. Fringes on the QUBIC TES array. *Left:* measured fringes corresponding to the baseline between horns 25 and 57. The fringes are clearly visible as bright, diagonal lines across the detector array. *Right:* simulation of the expected fringe pattern for the same baseline pair generated by `qubicsoft`. The measured fringe locations correspond with the simulated image. The amplitude of the fringe lines are expected to become fainter with distance from the centre of the focal plane. This was not measured because of saturation of the detectors. Pixel intensities are the same arbitrary units scaled to the peak of the measurement for both images.

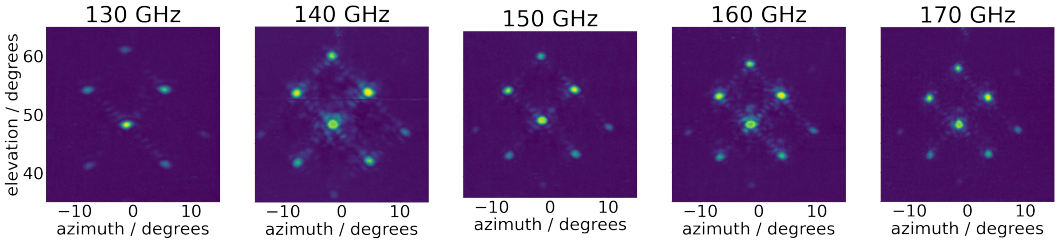

Figure 16. Measured maps of the synthesized beam for one TES detector. The multi-lobe synthesized beam is shown here for 130 GHz, 140 GHz, 150 GHz, 160 GHz, and 170 GHz. An animated version of this plot with comparison to simulation can be viewed online at https://box.in2p3.fr/index.php/s/bzPYfmtjQW4wCGj.

The result of the beam mapping measurement campaign is a series of maps for each TES pixel in the detector array. This is 244 maps for each frequency for a total of 1220 maps. Figure 16 shows example maps for one TES detector at five frequencies. The main lobe and secondary lobes are clearly visible and are at the expected locations. Figure 17 shows the maps of figure 16 in a single representation with three frequencies, 130 GHz, 150 GHz, and 170 GHz, assigned to colours red, green, blue.

The secondary lobe locations depend on the frequency of the incident radiation while the main lobe is always at the same place. Figure 17 shows a cut across the beam maps of figure 16. The secondary lobes are closer to centre for higher frequencies, as expected. This result is the first hardware demonstration of the capability of a bolometric interferometer to operate as a spectral imager (see Mousset et al. [11] for a detailed analysis).

4.5 Map making with measured synthesized beams

Using the relative location and amplitude of all the peaks in the synthesized beam for each of the TES, we can now project the data onto the sky using optimal map-making to deconvolve from the effect of the multiple peaks. In addition, by exploiting the spatial separation of secondary peaks and the dependence of their location on the frequency of radiation, the

JCAP04(2022)036

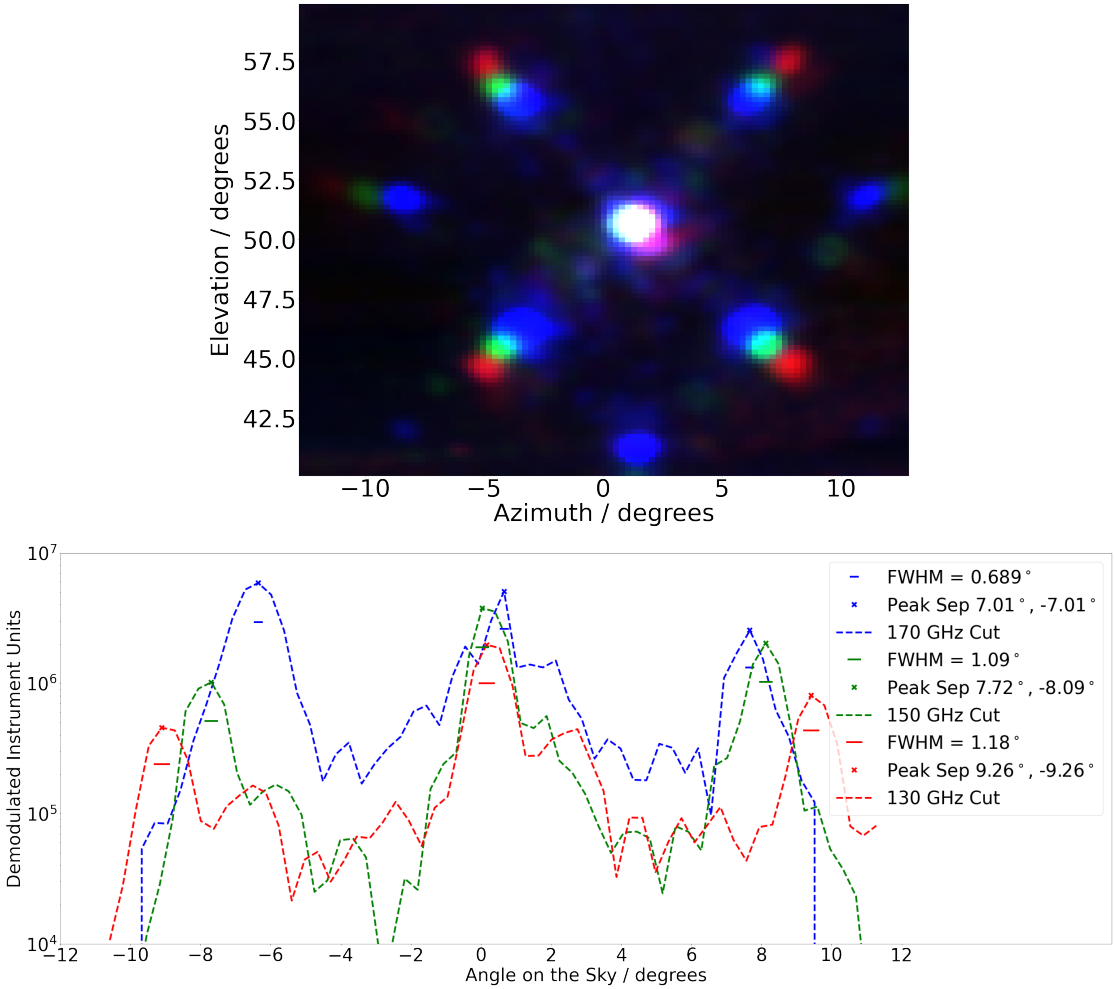

Figure 17. Multichroic representation of the maps of figure 16. Each frequency is assigned a colour, 130 GHz (red), 150 GHz (green), and 170 GHz (blue). The plot above shows the coincident central lobe for each frequency and the secondary lobes which are closer to centre as frequency increases. The plot below is the cross-cut along the diagonal from bottom-left to top-right of the image on the left. The peak at 170 GHz is truncated because of detector saturation.

analysis of the TOD leads to spectral imaging as described in detail in Mousset et al. [11]. Spectral discrimination is necessary to disentangle foreground contamination. When observing the sky, this will result in an unbiased CMB map as is shown using simulations in Mousset et al. [11].

We have performed this exercise with the calibration data in order to obtain an image of the point-like artificial calibration source projected onto a sky-map. The calibration source was set to emit at 150 GHz and using the alt-azimuth mount, QUBIC-TD was scanned across the source in azimuth and elevation. TOD are obtained for each bolometer. We then apply our spectral imaging map-making algorithm with five sub-bands to a selection of 26 bolometers that do not exhibit saturation. The synthesized beam for each bolometer is realistically modeled in our map-making through a series of Gaussian profiles whose amplitudes, widths and locations are fit from a measured map of the synthesized beam for each bolometer (see figure 16 for an example of the maps from one bolometer). The frequency evolution of this

JCAP04(2022)036

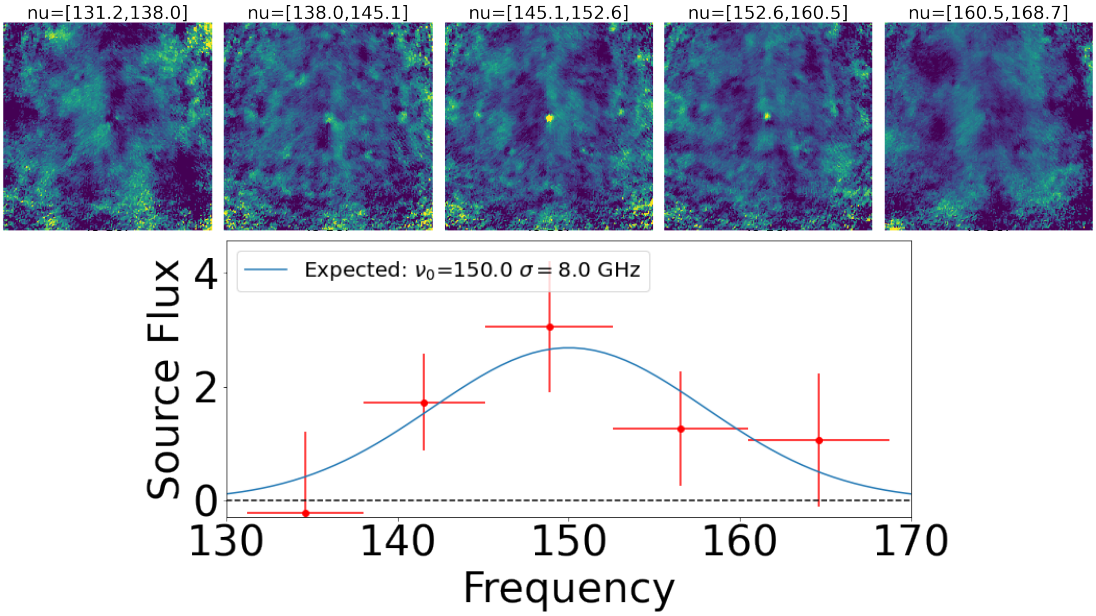

Figure 18. Calibration data with the source at 150 GHz projected on the sky using our map-making software to deconvolve from the multiple peaked synthesized beam and separate the physical band of the instrument into 5 sub-bands. The spectrum of the central pixel, in arbitrary flux units, is shown at bottom and matches the expected performance of spectral imaging by analysis of the TOD and applying the frequency dependence of the QUBIC beam as described in Mousset et al. [11].

synthesized beam assumes linear scaling with wavelength. We were able to reconstruct a map of the point-like artificial calibration source as well as its location in frequency space. The resulting image is shown in figure 18. The reconstruction onto 5 sub-bands exhibits the expected point-like shape in the central frequency sub-band containing the emission frequency of the source at 150 GHz. The calibration source, which was tuned to 150 GHz, is fainter in adjacent bands, and not visible in the furthest bands. Our measurement matches the spectral resolution predicted by the Rayleigh criterion (see Mousset et al. [11], section 3.2 equation 3.1) shown as the blue line in figure 18 (bottom).

The successful mapmaking with the measured synthesized beam is effectively an end-to-end checkout of the entire QUBIC system. In order for this exercise to be possible, all subsystems, interfaces between subsystems, and all associated software must be functioning correctly. This includes scientific and housekeeping data acquisition, telescope pointing control, and control and synchronisation of all subsystems. The software needed to make this measurement includes the system control software, the data acquisition software, data archiving and reading, and finally data analysis software together with comparison to system simulation software. The resulting map of figure 18 shows that all subsystems are functioning correctly, and all subsystems are correctly managed and synchronized together into the overall system.

5 Conclusion

QUBIC-TD underwent an extensive campaign of testing in the laboratory at APC in Paris. Using an artificial millimetre-wave source in the telescope far-field, functional tests were carried out and several performance parameters were successfully measured. Our measurement

JCAP04(2022)036

of the frequency-dependence of the synthesized beam is in excellent agreement with the theoretical prediction. This result, for the first time, opens up the possibility to use bolometric interferometry to perform spectral imaging. Based on these results, which were carried out on a single calibrating point source, preliminary simulations of QUBIC spectral imaging in presence of more realistic diffuse signals are very encouraging (Mousset et al. [11]). The spectral response has the required bandpass profile for operation in the 130 GHz to 170 GHz band. The polarization performance has less than 0.4% cross-polarization contamination at 150 GHz. These measurements confirm that bolometric interferometry is a viable method for the measure of CMB B-mode polarization. In particular, the measured polarization performance makes us confident that QUBIC will be one of the most competitive experiments in terms of polarization purity.

Deployment of QUBIC-TD on the scientific site of Alto Chorillo at 5000 m altitude in Argentina is expected by the end of 2022 for in-situ commissioning and preliminary data taking, as a precursor of the QUBIC full instrument. QUBIC will provide a clean polarization map of the sky and together with spectral imaging, will have excellent separation of foreground sources.

Acknowledgments

QUBIC is funded by the following agencies. France: ANR (Agence Nationale de la Recherche) 2012 and 2014, DIM-ACAV (Domaine d'Intérêt Majeur-Astronomie et Conditions d'Apparition de la Vie), CNRS/IN2P3 (Centre national de la recherche scientifique/Institut national de physique nucléaire et de physique des particules), CNRS/INSU (Centre national de la recherche scientifique/Institut national et al. de sciences de l'univers). Italy: CNR/PNRA (Consiglio Nazionale delle Ricerche/Programma Nazionale Ricerche in Antartide) until 2016, INFN (Istituto Nazionale di Fisica Nucleare) since 2017. Argentina: MINCyT (Ministerio de Ciencia, Tecnología e Innovación), CNEA (Comisión Nacional de Energía Atómica), CONICET (Consejo Nacional de Investigaciones Científicas y Técnicas).

D. Burke and J.D. Murphy acknowledge funding from the Irish Research Council under the Government of Ireland Postgraduate Scholarship Scheme. D. Gayer and S. Scully acknowledge funding from the National University of Ireland, Maynooth. D. Bennett acknowledges funding from Science Foundation Ireland.

References

[1] M. Kamionkowski and E.D. Kovetz, *The Quest for B Modes from Inflationary Gravitational Waves*, *Ann. Rev. Astron. Astrophys.* **54** (2016) 227 [arXiv:1510.06042] [INSPIRE].

[2] J. Kovac, E.M. Leitch, C. Pryke, J.E. Carlstrom, N.W. Halverson and W.L. Holzapfel, *Detection of polarization in the cosmic microwave background using DASI*, *Nature* **420** (2002) 772 [astro-ph/0209478] [INSPIRE].

[3] SPT-3G collaboration, *Measurements of the E-mode polarization and temperature-E-mode correlation of the CMB from SPT-3G 2018 data*, *Phys. Rev. D* **104** (2021) 022003 [arXiv:2101.01684] [INSPIRE].

[4] J. Alves, T. Forveille, L. Pentericci and S. Shore, *Planck 2018 results*, *Astron. Astrophys.* **641** (2020) E1.

[5] BICEP and Keck collaborations, *Improved Constraints on Primordial Gravitational Waves using Planck, WMAP, and BICEP/Keck Observations through the 2018 Observing Season*, *Phys. Rev. Lett.* **127** (2021) 151301 [arXiv:2110.00483] [INSPIRE].

JCAP04(2022)036

[6] QUBIC collaboration, *QUBIC Technical Design Report*, arXiv:1609.04372 [INSPIRE].

[7] QUBIC collaboration, *QUBIC VIII: Optical design and performance*, *JCAP* **04** (2022) 041 [arXiv:2008.10119] [INSPIRE].

[8] QUBIC collaboration, *QUBIC V: Cryogenic system design and performance*, *JCAP* **04** (2022) 038 [arXiv:2008.10659] [INSPIRE].

[9] QUBIC collaboration, *QUBIC IV: Performance of TES bolometers and readout electronics*, *JCAP* **04** (2022) 037 [arXiv:2101.06787] [INSPIRE].

[10] M.A. Bigot-Sazy, R. Charlassier, J.C. Hamilton, J. Kaplan and G. Zahariade, *Self-calibration: an efficient method to control systematic effects in bolometric interferometry*, *Astron. Astrophys.* **550** (2013) A59 [arXiv:1209.4905] [INSPIRE].

[11] QUBIC collaboration, *QUBIC II: Spectro-polarimetry with bolometric interferometry*, *JCAP* **04** (2022) 035 [arXiv:2010.15119] [INSPIRE].

[12] QUBIC collaboration, *QUBIC I: Overview and science program*, *JCAP* **04** (2022) 034 [arXiv:2011.02213] [INSPIRE].

[13] QUBIC collaboration, *QUBIC VI: cryogenic half wave plate rotator, design and performances*, *JCAP* **04** (2022) 039 [arXiv:2008.10667] [INSPIRE].

[14] G. Pisano, M. Ng, V. Haynes and B. Maffei, *A broadband metal-mesh half-wave plate for millimetre wave linear polarisation rotation*, *PIER M* **25** (2012).

[15] QUBIC collaboration, *QUBIC VII: The feedhorn-switch system of the technological demonstrator*, *JCAP* **04** (2022) 040 [arXiv:2008.12721] [INSPIRE].

[16] A. Schillaci, E. Battistelli, G. D'Alessandro, P. de Bernardis and S. Masi, *On the emissivity of wire-grid polarizers for astronomical observations at mm-wavelengths*, *Infrared Phys. Tech.* **58** (2013) 64 [arXiv:1212.3969] [INSPIRE].

[17] D. Burke, *Design and Analysis of the Optical Beam Combiner and Corrugated Feed Horns for the QUBIC Instrument*, *Maynooth Theses* (2021).

[18] A.C. Ludwig, *The definition of cross polarization*, *IEEE Trans. Antennas Propagat.* **21** (1973) 116.

[19] J.A. Hogbom, *Aperture Synthesis with a Non-Regular Distribution of Interferometer Baselines*, *Astron. Astrophys. Suppl. Ser.* **15** (1974) 417 [INSPIRE].

[20] D.N. Fort and H.K.C. Yee, *A Method of Obtaining Brightness Distributions from Long Baseline Interferometry*, *Astron. Astrophys.* **50** (1976) 19.

[21] A.C.S. Readhead and P.N. Wilkinson, *The mapping of compact radio sources from VLBI data*, *Astrophys. J.* **223** (1978) 25.

[22] T.J. Cornwell and P.N. Wilkinson, *A new method for making maps with unstable radio interferometers*, *Mon. Not. Roy. Astron. Soc.* **196** (1981) 1067.

[23] T.J. Pearson and A.C.S. Readhead, *Image formation by self-calibration in radio astronomy*, *Ann. Rev. Astron. Astrophys.* **22** (1984) 97 [INSPIRE].

[24] T. Cornwell and E.B. Fomalont, *Self-Calibration*, in *Synthesis Imaging in Radio Astronomy II*, G.B. Taylor, C.L. Carilli and R.A. Perley, eds., *ASP Conf. Ser.* **180** (1999) 187.

JCAP04(2022)036